DOI: 10.20350/digitalCSIC/15703

Electronic Supplementary Materials

to

Operando Exploration of Tribochemical Decomposition in Synthetic FeS_2 thin film and Mineral Iron Pyrite

E. Muñoz-Cortés,[a] J. Sánchez-Prieto,[b] B. Zabala,[c] C. Sanchez,[a,d] E. Flores,[e] A. Flores,[f] E. Roman,[g] J.R. Ares,[a] and R. Nevshupa[h]

[a] *MIRE-group, Departamento de Física de Materiales, M-4, Facultad de Ciencias, Universidad Autónoma de Madrid, Madrid 28049, Spain*

[b] *Centre for Microanalysis of Materials, Universidad Autónoma de Madrid, C/XX, Spain.*

[c] *Materials and Tribology unit, Tekniker, C/ I. Goenaga 5, Eibar, Spain.*

[d] *Instituto Nicolás Cabrera, Universidad Autónoma de Madrid, Francisco Tomás y Valiente 7, Madrid 28049, Spain*

[e] *Departamento de Física Aplicada, Centro de Investigación y de Estudios Avanzados (CINVESTAV), Mérida 97310, Mexico*

[f] *Departamento de Física de Polímeros, Elastómeros y Aplicaciones Energéticas, Instituto de Ciencia y Tecnología de Polímeros (ICTP), CSIC, C/ Juan de la Cierva 3, Madrid 28006, Spain*

[g] *Instituto de Ciencia de Materiales de Madrid (ICMM), CSIC, C/Sor Juana Inés de la Cruz 3, Madrid 28048, Spain*

[h] *Eduardo Torroja Institute of Construction Sciences (IETCC), CSIC, C/Serrano Galvache 4, Madrid 28033, Spain*

1. XRD of thin film and mineral pyrite

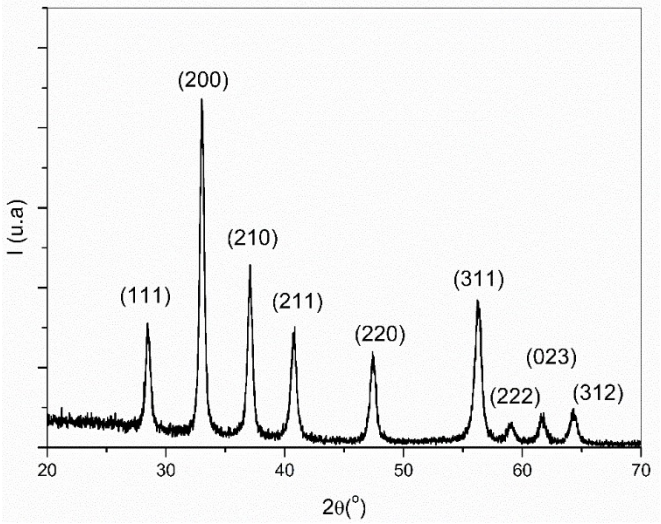

Fig. S1. Grazing-angle X-ray diffraction spectrum of obtained FeS_2 thin film. The corresponding crystal planes of iron pyrite are shown at each peak.

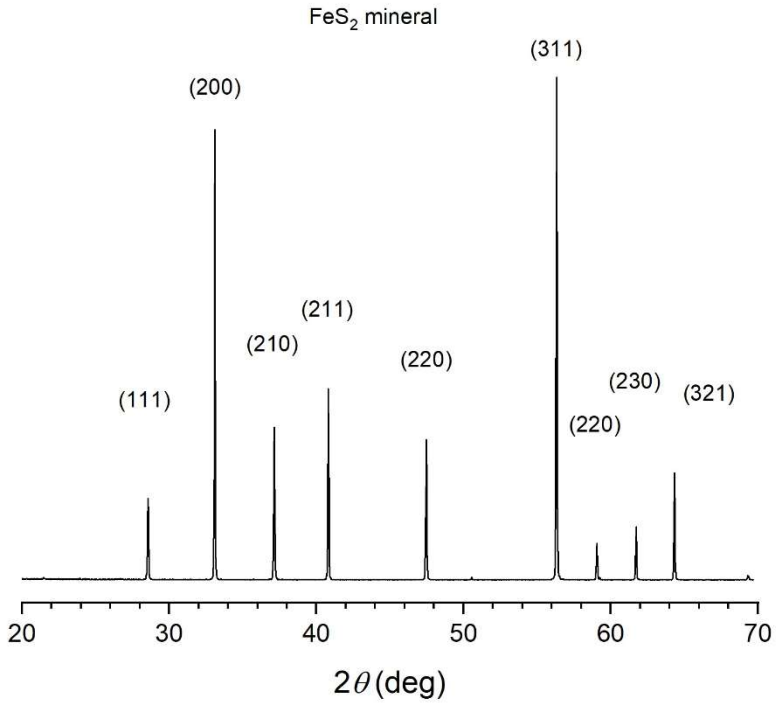

Fig. S2. X-ray diffraction patterns of mineral pyrite.

The XRD diagram of mineral pyrite shown in Fig. S2 perfectly matches the standard one (JCPDS No. 01-071-0053). The diagram of a thin-film sample shows all the main reflexes of mineral pyrite, but the relative intensities are slightly different. Furthermore, broadening of the peaks suggest a higher defect density and/or smaller grain size in the thin film.

2. Rutherford Backscattering Spectroscopy (RBS) and Elastic Recoil Detection Analysis (ERDA)

The samples were analyzed with RBS and ERDA methods (at 170° and 30° scattering angles, respectively) using two Si detectors (fixed and movable detector) simultaneously.

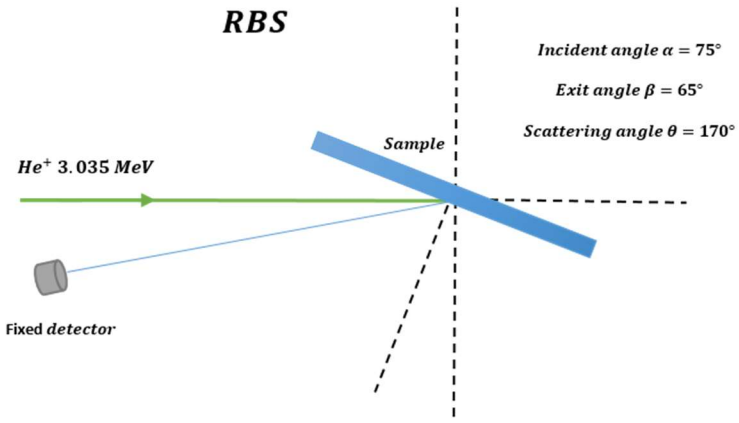

Fig. S3. Configuration of the RBS experiments under **O-resonance conditions** (3.035 MeV He^+ beam)

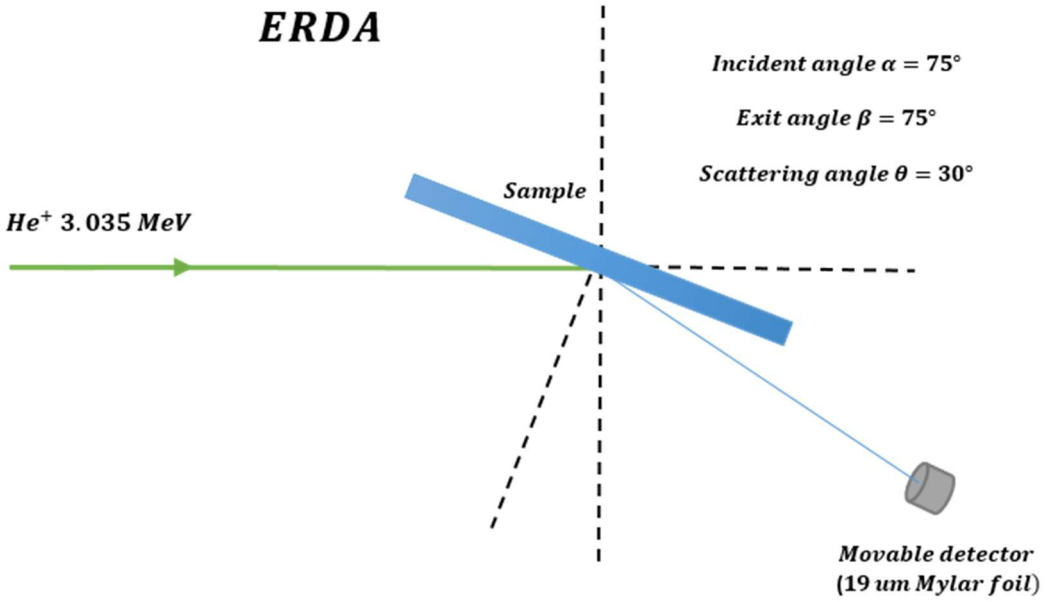

Fig. S4. Configuration of the ERDA experiments under **O-resonance conditions** (3.035 MeV He^+ beam)

The following figures show the experimentally measured data and fitting results, which were obtained using the calibration values 11.45 keV of energy offset and 2.23 keV of energy per channel.

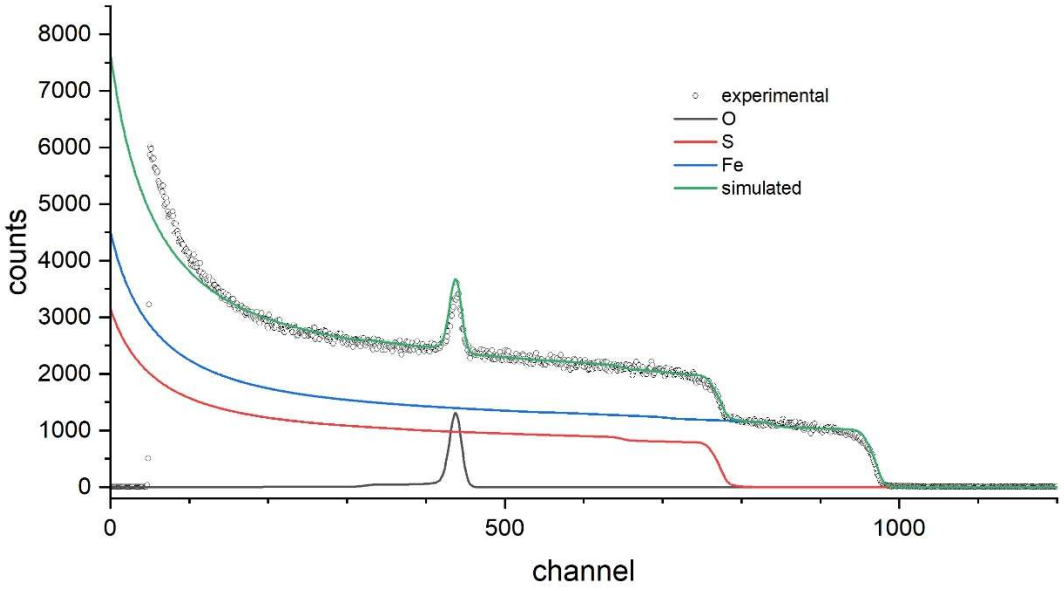

Fig. S5. RBS data and fitting results for mineral pyrite obtained under O-resonance conditions.

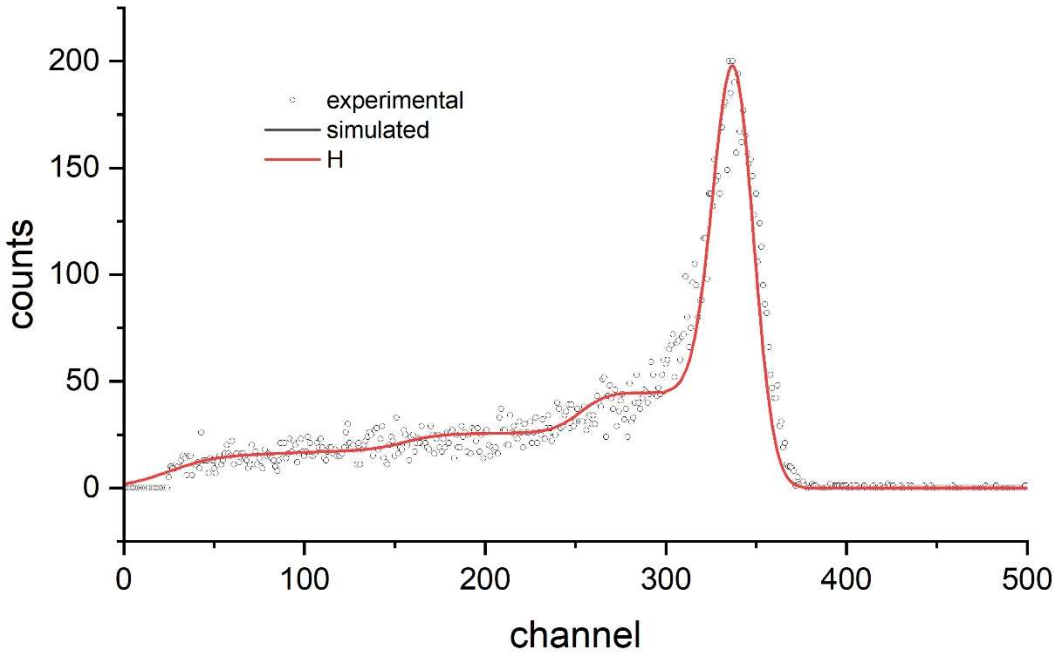

Fig. S6. ERDA data and fitting results for mineral pyrite obtained under O-resonance conditions

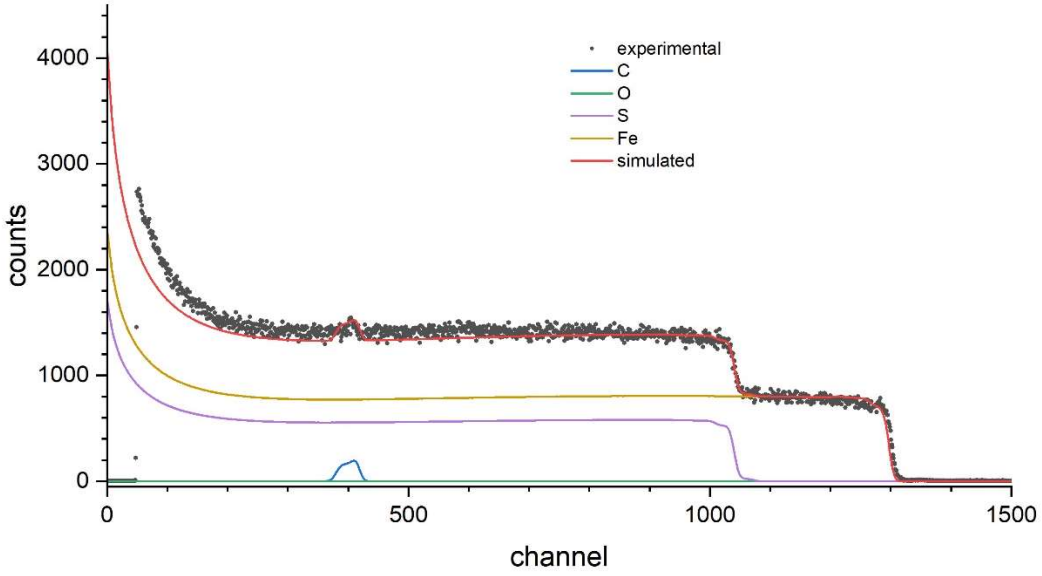

Fig. S7. RBS data and fitting results for mineral pyrite obtained under C-resonance conditions.

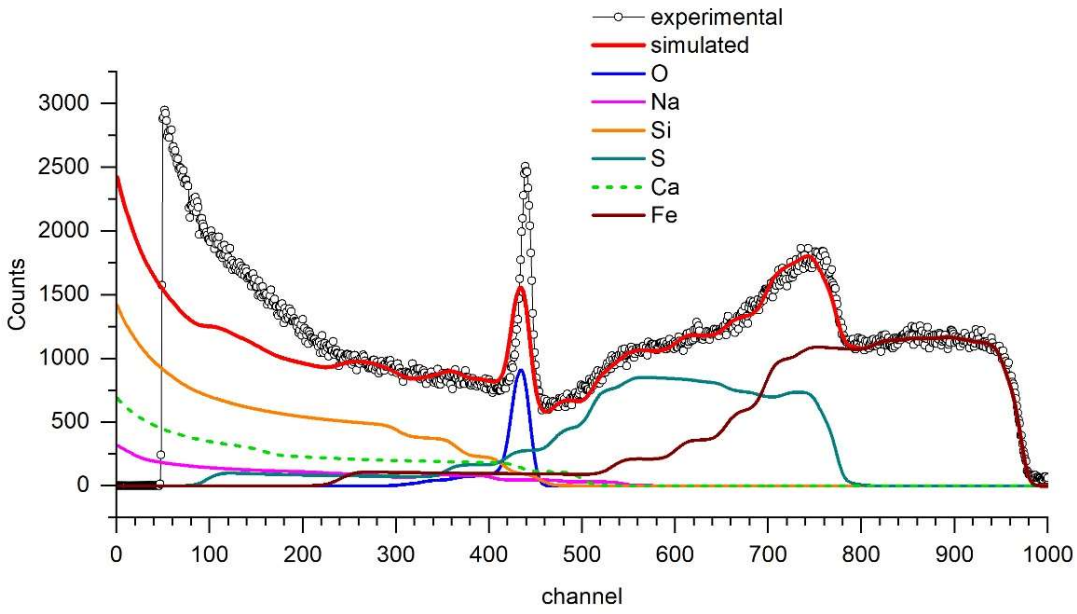

Fig. S8. RBS data and fitting results for thin film FeS_2 obtained under O-resonance conditions.

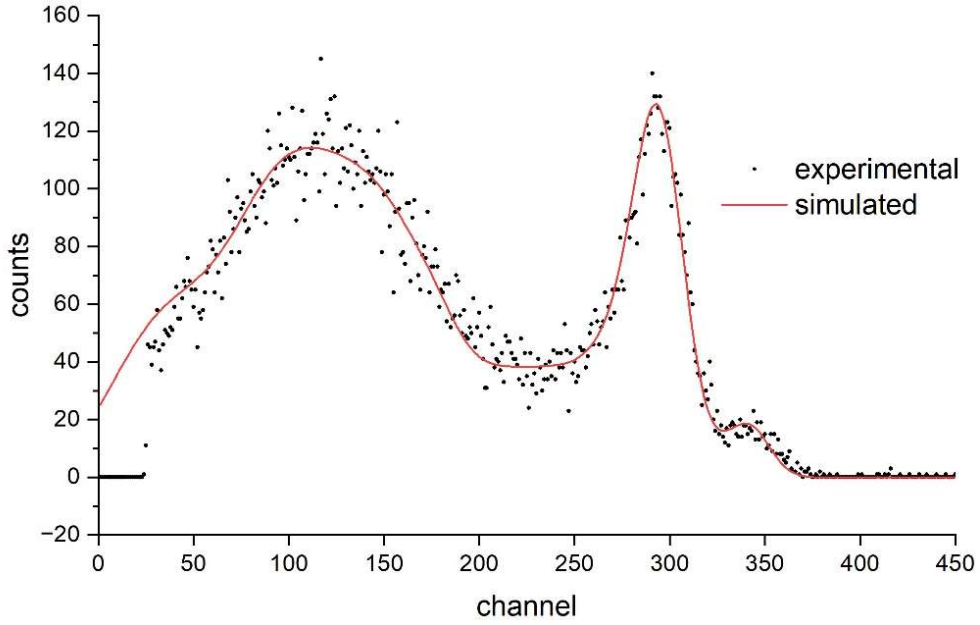

Fig. S9. ERDA data and fitting results for FeS_2 thin film obtained under O-resonance conditions.

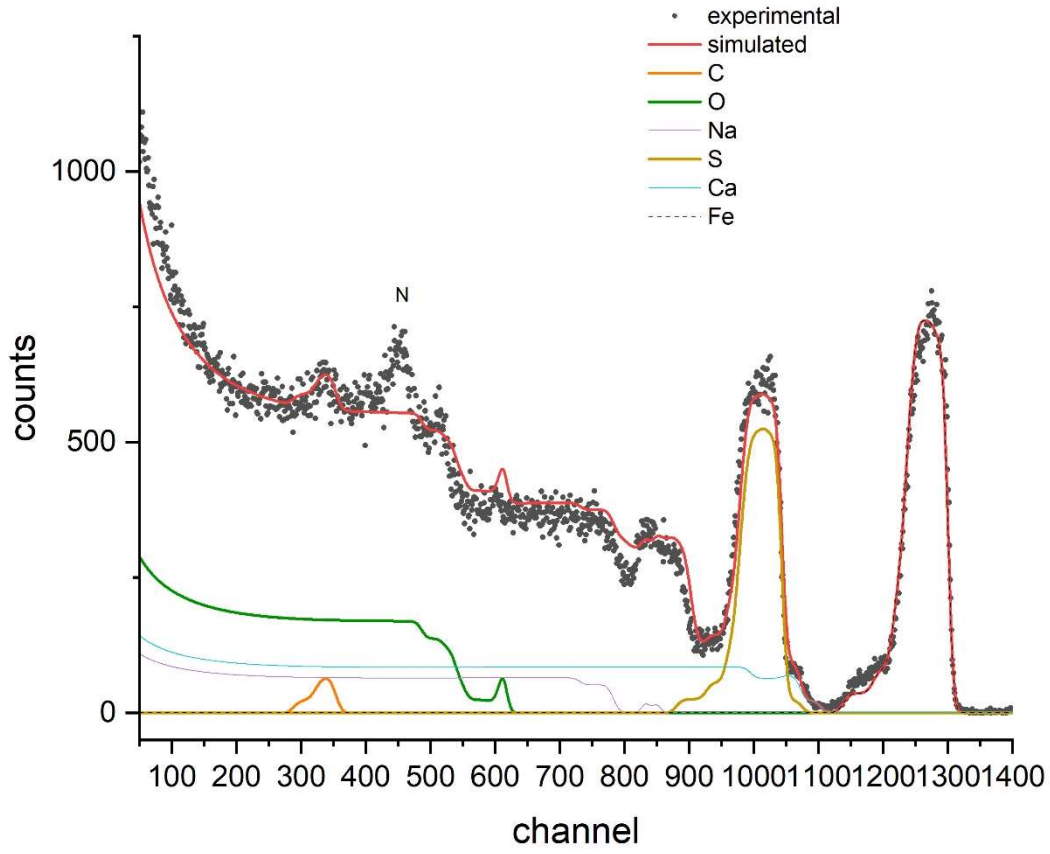

Fig. S10. RBS data and fitting results for FeS_2 thin film obtained under C-resonance conditions.

3. X-ray Photoelectron Spectrometry (XPS) of thin-film FeS_2

Table S1. The binding energies of various elements used for fitting of XPS spectra

Band		Bond energy (eV)	Possible chemical structure	References
Fe $2p_{3/2}$	Fe1	706.7 ± 0.2	Fe(II)(FeS_2) surface states	[1-5]
	Fe2	708.7 ± 0.3	FeS, FeOOH,FeO	[1, 4]
	Fe3	711.8 ± 0.5	αFe_2O_3, αFeOOH	[1, 2, 6]
S 2p	S1	160.8 ± 0.6	S^{2-} (FeS)	[1, 4, 7-9]
	S2	162.1 ± 0.1	S_2^{-2} (FeS_2)	[1-10]
	S3	164.0 ± 0.3	S^0, S_n^{-2}, $Fe_{1-x}S_2$	[1-4, 6, 7, 10]
	S4	168.2 ± 0.2	SO_4^{-2} ($Fe_2(SO_4)_3$, $FeSO_4$ $7H_2O$)	[2-5, 8]
O 1s	O1	529.7 ± 0.1	Fe_xO_y	
	O2	531.7 ± 0.1	O-H	
	O3	533.4 ± 0.1	H_2O, COH	
C 1s	C1	287.3 ± 0.1	C=O	
	C2	284.8 ± 0.1	C-C, C-H	
	C3	290.4 ± 0.1	carbonates	

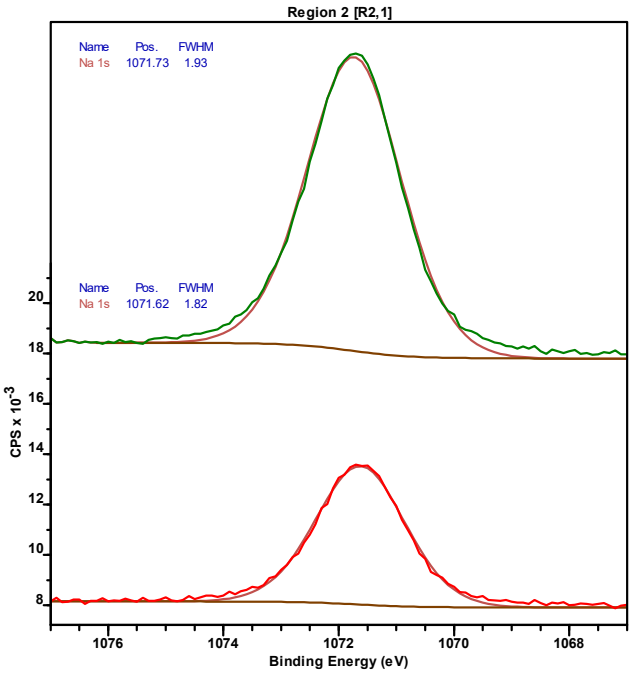

Fig. S11. XPS spectra of Na 1s: low part – before sputtering, upper part – after sputtering

4. Mechanically-Stimulated Gas Emission Mass Spectrometry (MSGE-MS)

Table S2. Assignment of the mass-spectrometry channels to possible ions

BP	*m/z*	Possible precursors and corresponding ionic fragments						
		C_xH_y	SO_x	H_2S	CO_x	COS	CS_2	S_x
α	12	C^+			C^+		C^+	
β	13	CH^+						
	14	CH_2^+						
	15	CH_3^+						
	16	CH_4^+	O^+		O^+	O^+		
	27	$C_2H_5^+$						
	28	$C_2H_4^+$			CO^+	CO^+		
	29	$C_2H_5^+$						
	30	$C_2H_6^+$						
	32		S^+	S^+		S^+	S^+	S^+
	33			HS^+				
	34			H_2S^+				
	44				CO_2^+	CS^+	CS^+	
	48		SO^+					
ξ	60					COS^+		
β	64		SO_2^+					S_2^+
δ	76						CS_2^+	
β	96							S_3^+

5. Electron stimulated desorption (ESD)

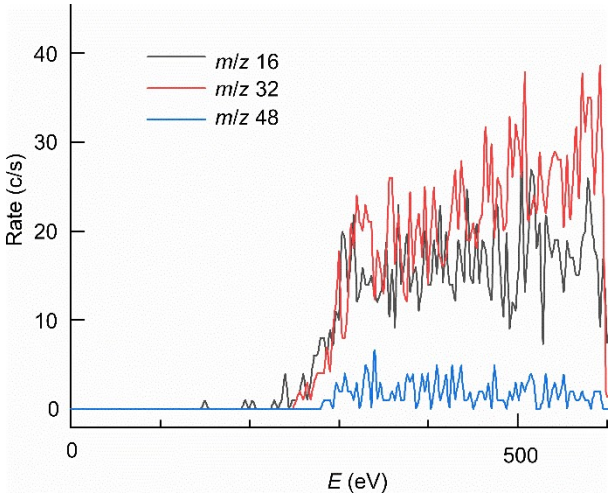

Fig. S12. The ion currents for ion emission at various *m/z* ratios as function of incident electron energy.

6. Thermal programmed desorption

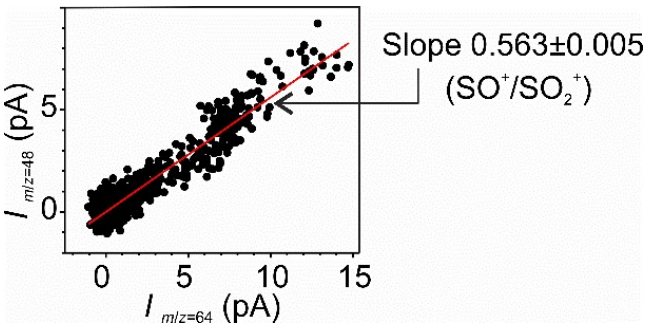

Fig. S13. Correlation between the mass-spectrometer signals at *m/z* 48 and 64 measured in the TPD experiments using a FeS_2 thin film at 20ºC/min in Ar.

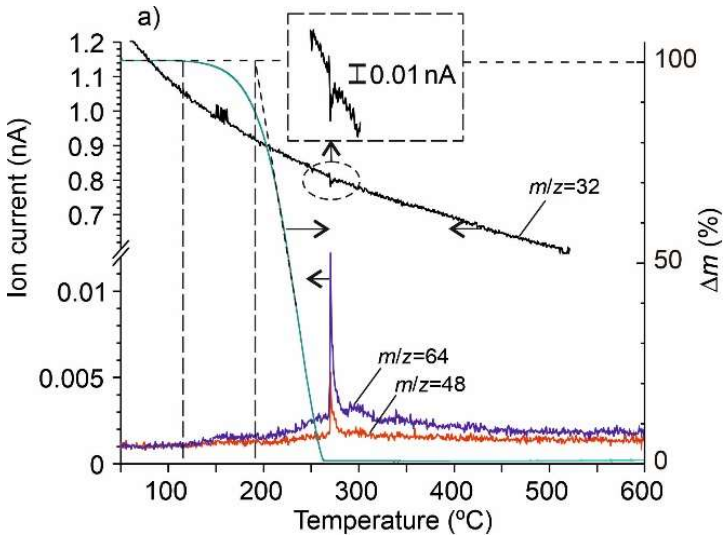

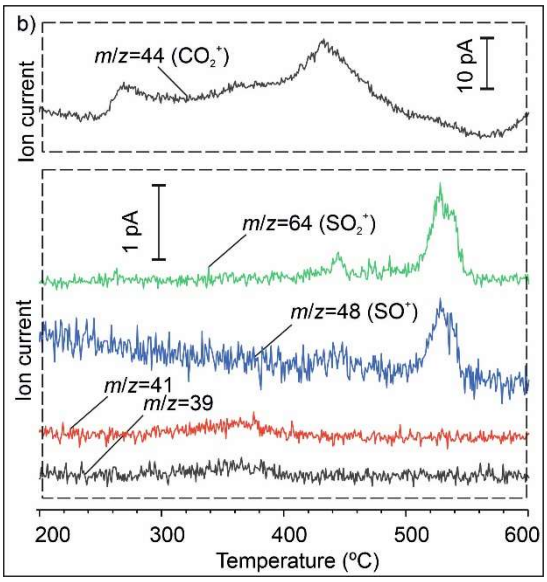

Fig. S14. a) TGA-MS results for elemental sulfur under linear heating rate 10 ºC/min under Ar; b) dry air flow, 10 ºC/min

Under a dry air flow, the peak of SO_2 thermal desorption shifted to higher temperatures. A broad peak at *m/z* 44, which was assigned to CO_2 and C3 hydrocarbons, was observed in the temperature range of 245 – 555 ºC. The assignment of *m/z* 44 to $CO_2^+/C_3H_8^+$ instead of CS^+ was supported by a synchronous but weak emission at *m/z* 22 (CO_2^{++}), 39 ($C_3H_3^+$) and 41 ($C_3H_5^+$) as well as the absence of emission at *m/z* 32 (S^+), 60 (COS^+) and 76 (CS_2^+).

7. Optical image and FTIR analysis of Mechanically Affected Zones (MAZ)

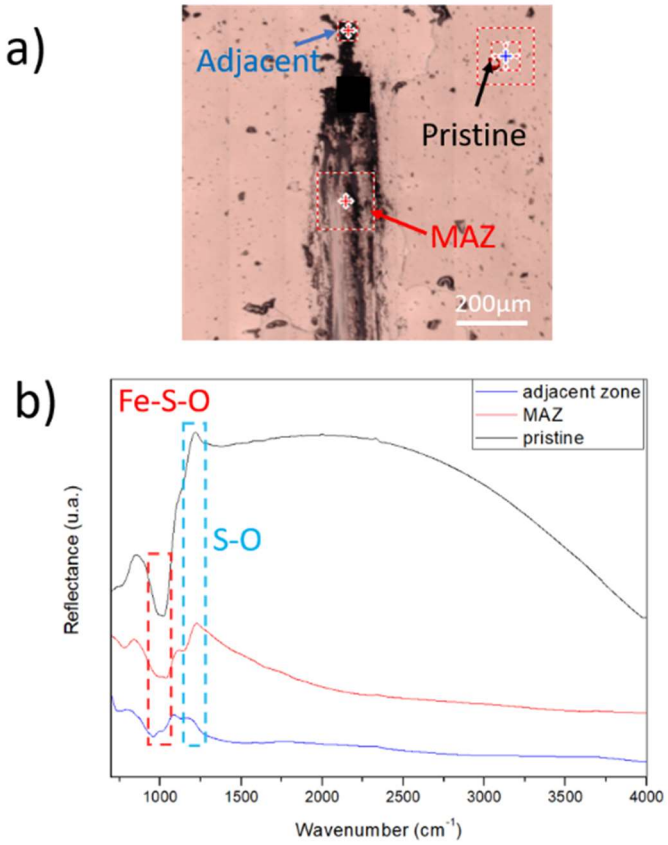

Fig. S15. a) Optical image of the sample surface after MSGE tests; b) the Infrared micro-reflectance spectra of non-affected region (pristine), mechanically affected zone (MAZ), adjacent zone. The band at 812 and 1330 cm^{-1} corresponds to asymmetric stretching of sulfur functional groups such as S-O. [11-16]

8. Nanoindentation

The elastic modulus was calculated following:

$$E_r = \frac{\sqrt{\pi}}{2\beta}\frac{S}{\sqrt{A}}, \quad (1)$$

where

$$\frac{1}{E_r} = \frac{(1-\nu^2)}{E} + \frac{(1-\nu_i{}^2)}{E_i}, \quad (2)$$

A is the projected contact area between indenter and sample, *S* is the contact stiffness, β is a correction factor (β = 1.034 for a Berkovich indenter) and E_r is the reduced elastic modulus accounting for the combined effect of sample and indenter. Equation 2 relates E_r to the elastic modulus and Poisson's ratio of the sample, *E* and ν respectively, and those of the indenter, E_i and ν_i respectively. It is assumed that E_i = 1141 GPa ν_i = 0.07 and ν = 0.15. The *A* function was calibrated for small penetration depths against a fused silica standard and such calibration yielded constant *E* values for $h \geq 20$ nm.

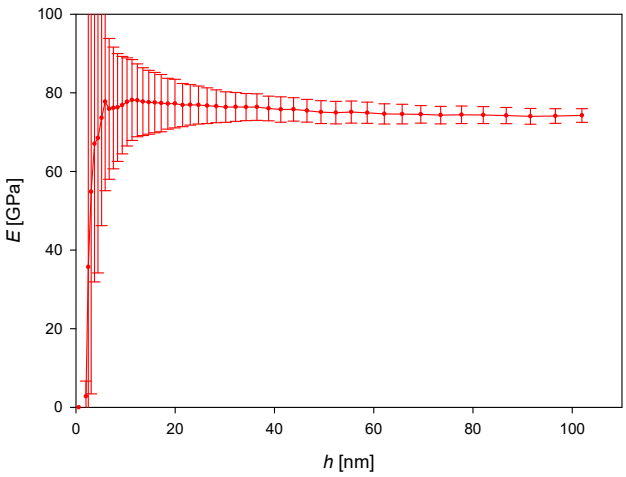

Figure S16. Young modulus as a function of indentation depth, for a fused silica standard.

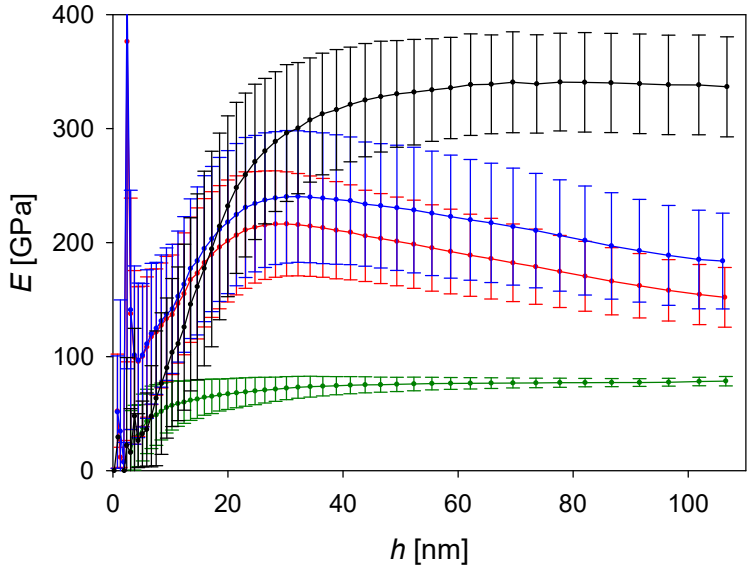

Figure S17. Indentation *E* values as a function of indenter displacement for: (•) natural pyrite; (•) polycrystalline pyrite thin film deposited on a glass substrate; (•) polycrystalline pyrite thin film deposited on a glass substrate, after correction for substrate contribution [8]; (•) glass substrate.

9. Model of heat dissipation at sliding interface

Approximate solution for flash temperature (circular contact on half-space):

$\Delta T_{max} = \frac{2 r \mu \sigma V}{\sqrt{\pi}\left(\lambda_1 + \sqrt{1+Pe_1} + \lambda_2\right)}$

where r is the size of the contact zone along the direction of sliding, μ is the friction coefficient, σ is the mean contact pressure, V is the sliding velocity, λ is the thermal conductivity, Pe_1 is the Peclet number for the flat sample:

$Pe_1 = \frac{V r \rho Cp_1}{2\lambda_1}$

Where ρ_1 ais the material density and Cp_1 is the heat capacity of the flat sample.

Subscripts 1 and 2 refer to the flat sample and the pin, correspondingly.

References

1. Eggleston, C.M., J.-J. Ehrhardt, and W. Stumm, *Surface structural controls on pyrite oxidation kinetics; an XPS-UPS, STM, and modeling study.* American Mineralogist, 1996. **81**(9-10): p. 1036-1056.
2. Brion, D., *Etude par spectroscopie de photoelectrons de la degradation superficielle de FeS2, CuFeS2, ZnS et PbS a l'air et dans l'eau.* Applications of Surface Science, 1980. **5**(2): p. 133-152.
3. Karthe, S., R. Szargan, and E. Suoninen, *Oxidation of pyrite surfaces: a photoelectron spectroscopic study.* Applied Surface Science, 1993. **72**(2): p. 157-170.
4. Nesbitt, H.W. and I.J. Muir, *X-ray photoelectron spectroscopic study of a pristine pyrite surface reacted with water vapour and air.* Geochimica et Cosmochimica Acta, 1994. **58**(21): p. 4667-4679.
5. Pratt, A.R., I.J. Muir, and H.W. Nesbitt, *X-ray photoelectron and Auger electron spectroscopic studies of pyrrhotite and mechanism of air oxidation.* Geochimica et Cosmochimica Acta, 1994. **58**(2): p. 827-841.
6. Buckley, A.N. and R. Woods, *The surface oxidation of pyrite.* Applied Surface Science, 1987. **27**(4): p. 437-452.
7. Zhu, J., et al., *Surface structure-dependent pyrite oxidation in relatively dry and moist air: Implications for the reaction mechanism and sulfur evolution.* Geochimica et Cosmochimica Acta, 2018. **228**: p. 259-274.
8. Schaufuß, A.G., et al., *Reactivity of surface chemical states on fractured pyrite.* Surface Science, 1998. **411**(3): p. 321-328.
9. Leiro, J.A., S. Granroth, and K. Laajalehto, *XPS study of the sulphur 2p spectra of pyrite.* Surface Science, 2003. **547**: p. 157-161.
10. Morales, C., et al., *An XPS investigation on the influence of the substrate and growth conditions on pyrite thin films surface composition.* Applied Surface Science, 2019. **492**: p. 651-660.
11. Dunn, J.G., W. Gong, and D. Shi, *A Fourier transform infrared study of the oxidation of pyrite.* Thermochimica Acta, 1992. **208**: p. 293-303.
12. Middya, S., et al., *Synthesis of Nanocrystalline FeS2 with Increased Band Gap for Solar Energy Harvesting.* Journal of Materials Science & Technology, 2014. **30**(8): p. 770-775.
13. Yani, S. and D. Zhang, *An experimental study into pyrite transformation during pyrolysis of Australian lignite samples.* Fuel, 2010. **89**(7): p. 1700-1708.

14. Venkateshalu, S., et al., *Solvothermal synthesis and electrochemical properties of phase pure pyrite FeS2 for supercapacitor applications.* Electrochimica Acta, 2018. **290**: p. 378-389.
15. Fathinia, S., et al., *Preparation of natural pyrite nanoparticles by high energy planetary ball milling as a nanocatalyst for heterogeneous Fenton process.* Applied Surface Science, 2015. **327**: p. 190-200.
16. Khataee, A., S. Fathinia, and M. Fathinia, *Production of pyrite nanoparticles using high energy planetary ball milling for sonocatalytic degradation of sulfasalazine.* Ultrasonics Sonochemistry, 2017. **34**: p. 904-915.